Inelastic Neutron Scattering Investigation of MgCl2Nanoparticle-Based Ziegler-Natta Catalysts for Olefin Polymerization

Inelastic Neutron Scattering Investigation of $MgCl_2$ Nanoparticle-Based Ziegler-Natta Catalysts for Olefin Polymerization

Maddalena D'Amore,[a,c,*] Alessandro Piovano,[a,b,c] Eleonora Vottero,[a,b,d] Andrea Piovano,[d] Svemir Rudić,[e] Alessandro Erba,[a] Elena Groppo,[a,b] and Bartolomeo Civalleri[a,b]

[a] Department of Chemistry and NIS Centre, University of Turin , Via P. Giuria 7, 10125 Torino, Italy

[b] INSTM, University of Turin, via G. Quarello 15/A, 101235 Torino, Italy

[c] DPI, P.O. Box 902, 5600 AX Eindhoven, The Netherlands

[d] Institut Laue-Langevin (ILL), 71 Avenue des Martyrs, 38042 Grenoble, France

[e] ISIS Facility, Rutherford Appleton Laboratory, Chilton, Didcot, Oxfordshire, OX11 0QX, UK

KEYWORDS Inelastic Neutron Scattering, Phonon dispersion, Quantum Mechanical Simulations, Nano-structuration, Heterogeneous catalysts, Inelastic Neutron Scattering, Phonon dispersion, QM simulations, Nano-structuration in catalysis, $MgCl_2$.

ABSTRACT: The effect of nanosize and structural disorder on the $MgCl_2$ support of Ziegler-Natta catalysts has been investigated in terms of induced changes to its vibrational spectroscopic fingerprint. In particular, the inelastic neutron scattering (INS) technique was used, which allowed sampling of the whole lattice dynamics of the support. The experimental INS spectra of several ball-milled, polycrystalline, samples of $MgCl_2$ were collected for the first time and were compared to simulated spectra from quantum-mechanical density functional theory calculations. Theoretical calculations were performed on a variety of $MgCl_2$ structural models: i) ordered and disordered bulk (3D); ii) low-dimensional structures such as surfaces (2D) and nano-rods (1D); and nano-clusters (0D). This allowed us to link specific features of the spectra to specific changes in the atomic structure and dynamics of the catalyst support. In particular, the effect of translational symmetry breaking and rotational disorder is discussed. Furthermore, the present data suggest that the ball-milling process mostly leads to the formation of bulk-like crystallites rather than nano-particles. This work ultimately highlights the combined use of INS measurements and quantum-mechanical simulations as an effective approach for the atomistic characterization of defective (nano)-materials.

1. Introduction

The loss of long range order (i.e. periodicity in at least one direction) in extended solids is a key feature that determines not only their intrinsic physical and chemical properties, but also their relevance for optical, electronic, magnetic and catalytic applications. [1,2] Therefore, there is much interest in finding synthetic procedures that enable full control of the shape - and thus properties - of nano-objects (such as surfaces, rods, nanotubes, nano-crystals).[3,4] Despite the great impact that nano-particles with controlled morphology had in many fields, it is still difficult to control, design or even predict their shape.[5,6,7,8,9]

The majority of industrial catalysts are constituted from high-surface-area supports with a nano-sized active phase dispersed on top. [10] The effect of particle size on the performance of the catalyst has motivated extensive studies on the fundamental aspects governing crystal growth. The concept of a thermodynamic “equilibrium shape" of nano-crystals, originally formulated by Wulff,[11] has recently been complemented with the analysis of the kinetic growth rate of different facets and the kinetics of transformation of a “growth shape” into the “equilibrium shape”, at a given temperature.[12,13] Another key factor that should be taken into account when referring to nano-catalysts is the effect of adsorbates, which may influence the relative stability of the catalyst nanoparticles exposed surfaces and lead, depending on the experimental conditions, to their reconstruction.[9],[14–17] A number of advanced experimental techniques have been developed for the direct (Transmission Electron Microscopy, TEM, and Scanning Tunneling Microscopy, STM) and indirect (X-ray based methods such as Small-Angle X-rays Scattering or X-ray Absorption Spectroscopy) characterization of the morphology of nano-particles.[13,18–21] Such developments progressively increased the resolution towards the atomic scale thus fostering the development of experimental tools suitable for the characterization of nano-catalysts in the presence of adsorbates. However, in most cases, a full elucidation of the structure-properties relation of these systems requires a complementary quantum-mechanical description.

The nano-sizing is not the only means to reduce the crystal periodicity. Disorder can have a similar effect. For example, the stacking faults commonly occur in crystals with close-packed lattices. For a regular cubic close-packed (ccp) lattice, the stacking sequence of the layers is ABCABCABC. However, the stacking faults can be introduced, disrupting the stacking sequence (e.g. ABCABABC). [22] Due to the typical low energy barriers for the incorporation or removal of these atomic planes, these defects can be easily formed.

Nano-size and disorder are key features of many catalysts and, among others, of $MgCl_2$-based Ziegler-Natta catalysts for olefin polymerization.[22–24] These catalysts represent the industrial evolution of ‘‘violet’’ (α, γ and δ) $TiCl_3$ polymorphs[25] for the production of isotactic polypropylene. In this context, we have recently performed a systematic study of a series of mechanically and chemically activated $MgCl_2$ nano-samples, aimed at analysing their structure, type and extent of disorder, size and morphology.[26,27] Quantum mechanical simulations suggested that stacking faults in $MgCl_2$ have a vanishing thermodynamic

cost.[27] The complementary use of powder X-ray diffraction (PXRD) and pair distribution function (PDF) analysis enabled the determination of the type and the extent of disorder.[26] Far-IR spectroscopy coupled with quantum-mechanical simulations and complemented by FT-IR spectroscopy of CO adsorbed at 100 K gave a comprehensive picture of the morphology of $MgCl_2$ nanoparticles and of their surface properties. [27]

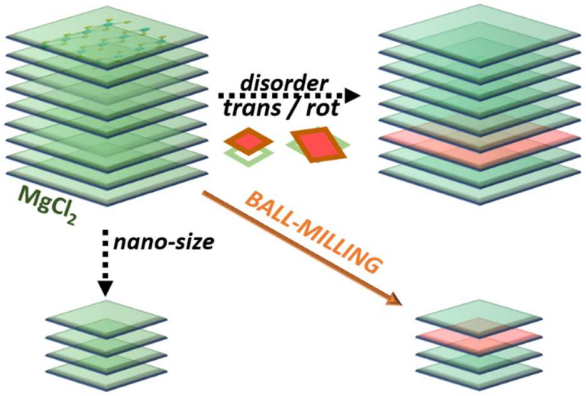

Scheme 1. Schematic representation of the synthesis process for the $MgCl_2$ investigated in this work and of the phenomena involved. Red layers indicate the insertion of disorder (either translational or rotational).

Herein, we extended that investigation by specifically looking at the lattice dynamics of $MgCl_2$ systems by means of Inelastic Neutron Scattering (INS) spectroscopy, which is a valuable method to probe the motion of atoms within a material and hence understand the structural disorder of nano-sized systems. INS measurements do not limit the sampling to the Brillouin zone centre – in contrast with other vibrational spectroscopies such as infrared and Raman - and they are not constrained by symmetry selection rules. This implies that all the vibrational modes are allowed and in principle visible in an INS spectrum, provided that the neutrons scattering cross-section of the species involved and the amplitude of motion of the atoms in the vibrational mode are sufficiently large. Neutrons deeply penetrate the matter for large distances before being scattered (or absorbed), so they ''see'' everything and the spectra are representative of both the bulk and the surface of the materials. As a consequence, the phonon modes of nano-crystalline domains may be different from those of bulk, since surface modes may be dominated by surface effects. [28]

The ability of INS to detect such surface effects resides in the choice of high surface area materials where the ratio of atoms at the surface and in the bulk is large. Although INS has been adopted to investigate a variety of materials, [29] it has been often overlooked in the field of catalysis, [30] mainly as a consequence of the poor range of sensitivity of the first neutron instruments. Only recently, has INS started to be applied to catalysts in the presence of adsorbates. Examples include the investigation of Pd- or Pt-based catalysts in the presence of hydrogen, [30–34] or the study of molecular mobility in zeolites. [35]

Despite the relatively large total scattering cross section of chlorine (16.8 barn), which makes it a suitable target for INS, the investigation of systems like $MgCl_2$ with neutron spectroscopy remains scarce.[36] Going beyond the target of a simple identification of chemical species through INS, the present study aims to show the potential of INS in the characterization of nano-sizing and disorder effects in $MgCl_2$-based materials. The analysis of experimental INS data is complemented with a detailed theoretical characterization by means of quantum mechanical calculations of several nano-sized and disordered models, that help provide insight into the origin of the observed changes in the INS spectra.

2. Methods

2.1. DFT modelling

All calculations were performed with the help of the periodic quantum mechanical CRYSTAL17 software. [37–40] Calculations were performed by using the B3LYP functional [41] augmented with a correction to include dispersion forces according to Grimme' s semi-empirical DFT-D2[42–44] approach with the empirical term refitted for crystalline systems.[45] TZVP quality basis sets have been employed for Mg atoms[46] and Cl atoms [47], except for the outer-most *sp* and *d* shells of Cl and Mg [48], where the exponents have been adjusted at the values reported in a previous paper by some of us from energy minimization of the cubic packed $MgCl_2$ α-form unit cell.[48,49]

Due to the size of the atomistic models investigated in the present work (vide infra), the massively parallel distributed data version of the code (MPPCrystal) has been employed, which features an excellent strong scaling due to the very high degree of parallelization of the code. [40,50] A reduced required memory per core is also a valuable feature of the present code. Both these features are key for an effective quantum-mechanical investigation of large systems (containing several hundreds or thousands of atoms per cell), with little or no point-symmetry. Calculations were performed at the SuperMUC phase-1 (LRZ, Germany) HPC IBM iDataPlex machine powered by 16 Intel cores per node running at 2.7 GHz, with 2GB/core and SCARF facilities at Rutherford Appleton Laboratories. The largest calculations were run on 1024÷2048 cores.

Pack-Monkhorst grids [51] for sampling the reciprocal space were used. These consisted of at least 16 **k**-points in the First Brillouin Zone, depending on the examined system (further details are provided later on and in the Supporting Information section for each model system).

The truncation of the Coulomb and exchange infinite lattice series is controlled by five thresholds T_i (see CRYSTAL17 manual for more details), which have been set to 8 (T_1–T_4) and 16 (T_5). The convergence threshold on energy for the self-consistent field (SCF) procedure has been set to 10^{-8} Ha for the structural optimization, and to 10^{-13} Ha for the vibration calculations. Full relaxation of internal coordinates and cell parameters has been carried out.

2.2 Vibrational frequencies and phonon modes

Harmonic phonon frequencies ω_p at the Γ point (i.e. the center of the first Brillouin zone, FBZ, in the reciprocal space) were obtained from the diagonalization of the mass-weighted Hessian matrix of the second energy derivatives with respect to atomic displacements *u* by using algorithms implemented in the CRYSTAL program. [52,53]

Sampling of phonon dispersion inside the FBZ is obtained by building and diagonalizing a set of dynamical matrices for a set

of **k** points in the FBZ. A "direct space" approach [54–57] is here used, which allows to build such dynamical matrices from a Fourier transform of the elements of direct space Hessian matrices computed within a super-cell, SC, of the crystallographic cell. From the diagonalization of dynamical matrices, normal modes and corresponding vibrational frequencies are sampled over the FBZ.

Long-range electrostatic contributions to the force constants are accounted for by means of an approach presented by Wang and collaborators [58] in combination with Fourier interpolation. This mixed-space approach is implemented in CRYSTAL for 3D periodic systems and has been documented to provide accurate phonon dispersions and phonon density of states (PDOS) for systems of different symmetries. [58] For low-dimensional periodic systems (< 3D) only a direct method has been applied involving the adoption of larger super-cells to fully-converge the long-range electrostatic terms. Systems under investigation have periodicity ranging from 3D to 0D and both ordered and disordered 3D systems have been considered. For calculating the force constants in real space, 3×3×3, 3×3×4, 4×4×2 super-cells have been adopted for the ordered hexagonal cell of α-$MgCl_2$ and disordered bulk models as reported by some of us in a previous paper.[27] To further check the numerical accuracy of our computational approach, test calculations were performed with different basis sets, and Fourier and Wang [58] interpolation parameters on smaller 2×2×2 super-cells. Heyd and Peintinger [59] basis set, along with a customized basis set (see Table S-1 in the Supporting Information).

2.3 Simulation of the INS spectra

Our data include both coherent and incoherent scattering from samples that are both polyatomic and polycrystalline. In the case of scattering from single crystals, the scattering vector $\boldsymbol{Q}$ has a definite orientation with respect to the reciprocal space of the single crystal, while in powder samples, the averaging over the various grains is equivalent to averaging over all orientations of the scattering vector. In the incoherent approximation,[60] it is proposed that the rotational averaging due to the powder nature of the sample cancels out correlations between distinct atoms. This approximation brings to the following formulation of the neutron scattering function:

$$S_{inc}(Q,\omega) = exp\left(-2\overline{W}(Q)\right)\frac{Q^2}{\hbar\omega}\langle n+\frac{1}{2}\pm\frac{1}{2}\rangle\left[\sum_a \frac{\sigma_a^{scatt}}{2M_a} g_a(\omega)\right]$$

where $g_a(\omega)$ is the atomic partial density of state. With this, much simpler, expression we can transform our (Q, ω) dataset into the phonon density of states, only supplying the mean-squared displacement and atomic composition. The neutron–weighted phonon density of states is the sum of the partial components of the density of states weighted by the scattering cross section integrated over all Q. This may not find a complete correspondence with the experimental data obtained on the instrument where Q is limited to specific values, but the approximation generally does not sensibly modify the relative peak intensities and does not affect difference spectra. The consistent application of such an approximation to all simulated spectra may keep their quantitative comparison valuable.

A detailed treatment of neutron scattering for single crystal and polycrystalline samples can be found elsewhere.[61]

Neutron weighted phonon density of states are here computed quantum-mechanically from the full phonon dispersion of the different models.[62,63] The total phonon density of states is defined by the formula:

$$g(\omega) = \frac{1}{V_{BZ}}\int_{BZ}\sum_{p=1}^{3N}\delta(\omega_{\boldsymbol{k}p}-\omega)d\boldsymbol{k}$$

where V_{BZ} is the volume of the Brillouin zone and N is the number of atoms per crystallographic cell, so that $\int g(\omega)d\omega = 3N$. This total density of states can be partitioned into atomic contributions: $g = \sum_a g_a(\omega)x_a$. For each atomic species a present in the system with a fraction x_a, the corresponding contribution is $g_a(\omega) = \frac{1}{n_{\boldsymbol{k}}}\sum_{p,\boldsymbol{k}}\left|e_{p,\boldsymbol{k};a}\right|^2\delta(\omega_{\boldsymbol{k}p}-\omega)$

Where $e_{p,\boldsymbol{k};a}$ are the eigenvectors of the dynamical matrices.

A neutron-weighted phonon density of states (NWPDOS) can be defined as [62]:

$$g^{NW}(\omega) = C\sum_a \frac{\sigma_a}{M_a} g_a(\omega)x_a$$

Where C is a normalization factor to satisfy $\int g^{NW}(\omega)d\omega = 3N$, and where each atomic species is weighted by a factor that is the ratio of the corresponding scattering cross section and mass.[64] A thermal correction to the computed NWPDOS is not applied because the comparison is performed with experimental spectra recorded at 15 K.

Due to the different ratios $\frac{\sigma_a}{M_a}$ for Mg and Cl of 0.15 barn mol/g and 0.39 barn mol/g, respectively, the spectra are dominated by Cl atoms.

The normal modes are analysed and those largely involving Cl atoms used to characterize the spectral features due to bulk, surfaces and/or border atoms.

Finally, the energy resolution in the experimental measurements would affect the comparison with computed NWPDOSS we are going to show in section 4.3, hence similarly to what can be done on S(Q, ω) by Mantid[65] for indirect-geometry instruments such as TOSCA, the simulated data were convolved with an experimental resolution function $f(\omega)$ of the form:

$$f(\omega) = \frac{1}{\sqrt{2\sigma^2(\omega)\pi}}exp\left(-\frac{1}{2}\frac{\omega^2}{\sigma^2(\omega)}\right)$$

where:

$$\sigma(\omega) = A\omega^2 + B\omega + C$$

A, B, C being instrument dependent constants.

3. Experimental details

Three $MgCl_2$ samples characterized by increasing surface area were measured. A highly crystalline $MgCl_2$ sample was donated by Toho Titanium Co., Ltd. ($MgCl_2$ A, specific surface area (SSA): 9.3 m^2/g). $MgCl_2$ B and $MgCl_2$ C were obtained by planetary ball-milling the initial highly crystalline $MgCl_2$ A sample for different times, resulting into SSA of 55 m^2g^{-1} and 73 m^2g^{-1}, respectively. The same three samples have been the subject of a detailed characterization in our previous works,[26,27] ensuring high purity and good reproducibility. In particular, according to the structural analysis in Ref. 34, the average dimensions of $MgCl_2$ particles are 55×55×42 nm^3 in A, 16×16×13 nm^3 in B, and13×13×8 nm^3 in C.

The experimental INS spectra were recorded at 15 K using the TOSCA spectrometer at the ISIS spallation Neutron and Muon

Source (Rutherford Appleton Laboratory, UK)[32,66,67,] with a ΔE/E resolution of 2 %. The samples were inserted in a thin aluminum envelope and placed into In-wire sealed Al cells. All the manipulations were performed inside a glove-box to prevent contamination by moisture. The cell was then inserted in a duplex CCR cryostat and cooled down. The INS signals from sample scattered neutrons were recorded by detectors both in forward and in backward directions for about 10 hours per sample, then they were extracted and combined using Mantid software.[65] The neutron beam area at the sample position is 45 mm × 45 mm ensuring that the whole sample contained within aluminum envelope was measured. The spectra were normalized in relation to sample mass (ca. 7 g per sample) and incoming proton current (ca. 2000 μA per sample) values, in order to allow a quantitative comparison.

4. Results and Discussion

In the following, we will first discuss the experimental INS spectra of three $MgCl_2$ samples having a progressively increasing specific surface area. Then, the *ab initio* simulated INS spectra obtained for different $MgCl_2$ model systems will be presented, starting from the bulk and ordered α-$MgCl_2$ model and moving to models that account for disorder effects in the bulk and nano-sizing effects (2D, 1D and 0D models).

4.1 Experimental INS spectra

Figure 1 shows the experimental INS spectra of $MgCl_2$ A, $MgCl_2$ B and $MgCl_2$ C. The three spectra have been normalized to the sample mass. In order to highlight the effect of ball milling on the spectral features, Figure 1 reports also the difference spectra (ΔS(Q, ω)) obtained by subtracting to the spectra of $MgCl_2$ B and $MgCl_2$ C by their respective preceding one in the series. The largest part of information in the plot of total S(Q, ω) vs. energy transfer falls in the 60 – 400 cm^{-1} range, where several well defined bands are observed at ~100 cm^{-1} (doublet), 162 cm^{-1} (with a shoulder at ~170 cm^{-1}), 200 cm^{-1}, 236 and 251 cm^{-1}.

At a first glance, INS spectra appear much richer in details than the corresponding Far-IR spectra, [27] which are dominated by a very broad band centred at ~243 cm^{-1}, with a shoulder at 295 cm^{-1} and two weaker bands at ~370 and 410 cm^{-1}. Far-IR spectroscopy turned out to be sensitive to the morphology of the $MgCl_2$ nanoparticles (i.e. to the relative extent of the exposed surfaces), while quantum mechanical simulation revealed that it was almost insensitive to the $MgCl_2$ disorder.[27] The unprecedented detail of our INS spectra together with the newly performed simulations will now permit to complement and extend our previous work shedding light on the disordering and nanostructuration effects.

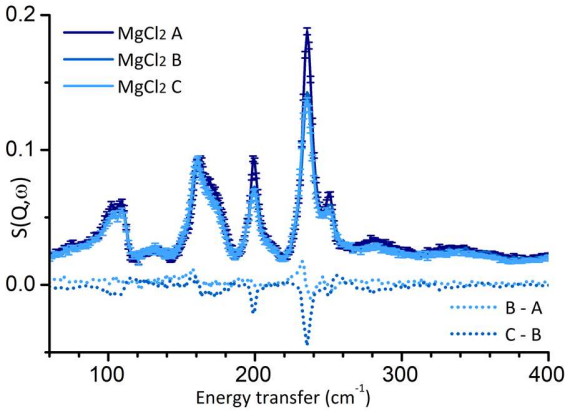

Figure 1. INS spectra of $MgCl_2$ A, $MgCl_2$ B, $MgCl_2$ C samples and their differences. See the text for further details.

All the INS bands are sensitive to a different extent to the ball milling time and either decrease in intensity or slightly shift in position (or both) by moving from $MgCl_2$ A to $MgCl_2$ C. The most affected bands are those at 200, 236 and 251 cm^{-1}, which decrease in intensity at longer ball milling times. It is widely recognized [22,23,26,68] that increasing the ball milling time brings about an increase in $MgCl_2$ disorder (introducing both stacking and rotational disorder), a decrease in the particle size and a change in morphology (i.e. in the type and relative extent of the exposed surfaces). In order to understand which one of these three effects mainly affects the INS spectrum of $MgCl_2$ we underwent a comprehensive quantum mechanical computational work.

4.2 Simulation of the INS spectra: atomistic models and approach

We considered various atomistic models of decreasing dimensionality (from 3-D and 0-D models) that mimic disorder and nano-sizing effects. More in detail, by starting from the crystalline structure of α-$MgCl_2$, two types of disorder were simulated (Figure 2A), as already done in our previous work [27]: a) a translational stacking fault was simulated by alternating layers of α-$MgCl_2$ (which has a ABCABC sequence) with layers of β-$MgCl_2$ (having a ABABAB sequence), to create the δ_{trans} form [22,24,68]; b) a rotational disorder was simulated from α-$MgCl_2$ by a simple rotation of one layer of 60° around the *c* axis, resulting into the δ_{rot} model. 2-D systems were modelled as slabs of well-defined thickness, as described in previous papers by some of us. [9,48,69] Slab models were built to simulate $MgCl_2$ surfaces of interest for their role in Ziegler-Natta catalysts, namely the (104) and (110) faces, along with the ubiquitous basal (001) one (Figure 2B).

To model the presence of edges in nano-sized catalysts, the (110)/(104) edge was also explored, by creating a 1-D infinite rod generated by intercepting the two faces (Figure 2C). Finally, a nanocrystal (formed by 240 atoms) having the crystalline structure of $MgCl_2$ but a finite size was also modelled (Figure 2D). The model was designed by cutting the α-$MgCl_2$ crystal according to the Wulff polar plot predicted for α-$MgCl_2$ on the basis of the Gibbs free energy of formation of surfaces (G_s). This nanocrystal represents a model for the most stable thermodynamic morphology at 298 K.[3] The polyhedron has been obtained by cutting the crystal along the largest extended families

of planes (104), (012), (001) with further cuts along (110) planes that are supposed to be the theatre of catalysis.

All the model systems investigated in the present work are expected to be representative of typical local structures occurring in $MgCl_2$ adopted in Ziegler-Natta catalysis.

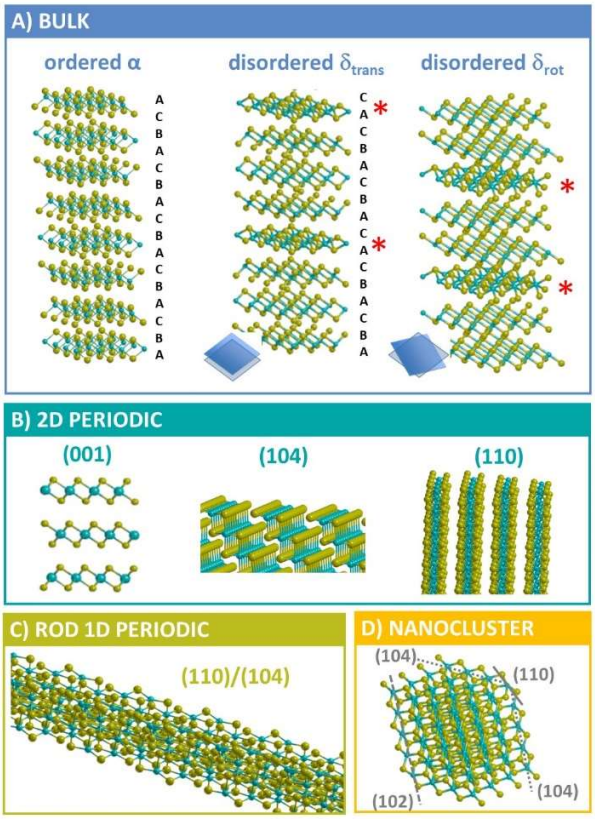

Figure 2. Ordered and disordered 3D models for $MgCl_2$ (panel A) as well as low-dimensionality models ranging from 2D to 0D adopted for simulating the INS spectra. In models of disordered δ forms, the faults have been indicated by red asterisks. Panel B) reports main surfaces of interest in catalytic processes (110) and (104) together with the basal (001) surfaces; whereas in panel C) a polymeric model (i.e. 104/110 rod) is reported. The nanocluster in panel D) is obtained according to the Wulff's polar plot as already reported in reference.[27] All structures represent local topologies typical of poly-crystalline $MgCl_2$ adopted in Ziegler-Natta catalysis.

4.3 Prediction of INS spectra for ordered and disordered bulk $MgCl_2$

The simulation of an INS spectrum for a crystalline material requires the calculation of the vibrational spectrum in reciprocal space points other than Γ from the Hessian matrix on a supercell of the original primitive cell. To achieve well-converged neutron spectra that can be reliably compared to the experimental ones we have to decide how much dense the reciprocal space sampling need to be. Such convergence trend is analyzed in this work as a function of the number of **k**-points used for integration in the reciprocal space. The method implies the construction of consistent supercells in each case. On this purpose, for ordered α-$MgCl_2$ (the most stable polymorph of $MgCl_2$ at TPS), phonon dispersion calculations have been performed on supercells of increasing size, namely 2×2×2 (72 atoms), 3×3×3 (243 atoms), 3×3×4 (324 atoms) and 4×4×2 (288 atoms). Computational details are reported in Table S-1 in Supporting Information.

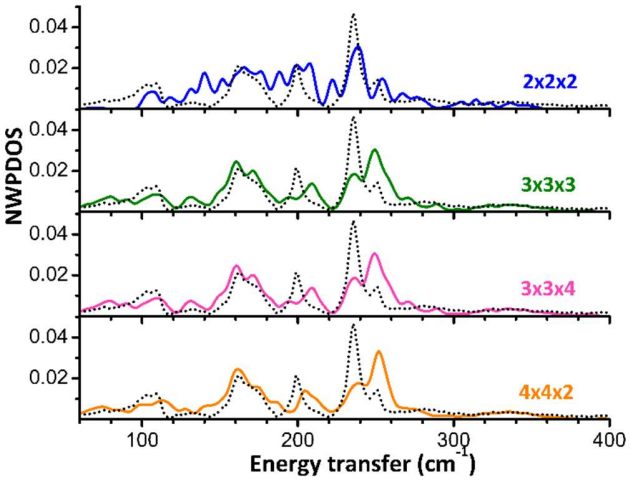

Figure 3. Neutron-weight corrected DOS (full lines) simulated for ordered bulk α-$MgCl_2$ by means of supercells of increasing size, compared to the experimental INS spectrum of $MgCl_2$ B (dotted line).

Figure 3 shows the neutron-weighted phonon density of states for ordered α-$MgCl_2$ simulated for different supercells of increasing dimension, compared to the experimental INS spectrum of $MgCl_2$ B. With the only exception of the spectrum obtained for the smallest 2×2×2 supercell, which shows a much larger number of bands than the experimental one, the other models consistently describe the experimental scattering function in terms of number of bands and position, while there are some discrepancies in terms of their relative intensities. In particular, the intensity of the band at 236 cm^{-1} is underestimated, while that of the band at 251 cm^{-1} is overestimated, resulting in an inversion in the relative intensity of the two bands with respect to the experimental spectrum. Higher order effects, such as contributions from second- and third-overtones, are negligible and do not affect the profile of the INS spectra in this region (see Figure S-2 ÷ Figure S-4 in Supporting Information). In contrast, the prediction of the stacking can be more relevant than expected, so that motion of the atoms might be influenced by the description of the weak interactions that take place among layers and might also suffer from the underestimation of the *c* cell parameter due to the adopted computational methodology.

The main bands observed in the experimental INS spectra are ascribed to the vibrational modes sketched in Figure 4, as follows.

i) The doublet at ~100 cm^{-1} (Figure 4A) is due to the "Raman active" displacement of the magnesium cation (Mg_1) in phase with two chlorine ligands (Cl_2 and Cl_3) along the *b* direction and to the analogous "IR active" vibrational mode. The atoms displacements by breaking the axial Mg-Cl bonds (i.e. Mg_1-Cl_4) would leave Mg ions binding four Cl ligands in the plane and would allow the creation of nano-ribbons of $MgCl_4$. The displacement of atoms in one layer (L_0) is opposite to that of the atoms belonging to adjacent layers (L_{-1} and L_1). The band arises when k points other than the Γ point are considered, and this explains why this band was not

discussed in the paper of Brambilla et al., reporting the IR and Raman experimental vibrational frequencies of $MgCl_2$.[70]

ii) The band at 162 cm^{-1} (Figure 4B) involves the intra-layer deformation of a 4-membered Cl-Mg-Cl-Mg rings with a stretching in the *ab* plane; more in details, in layer L_0 an in phase shortening of Mg_1-Cl_2 and Mg_1-Cl_3 bonds produces the rings' deformation, whereas in the adjacent layer L_{-1} a rotation around the Mg_4Mg_5 axis occurs with a deformation of Cl-Mg-Cl-Mg ring in the *ab* plane. The vibrational modes of layers L_0, L_{-1} and L_1 are coupled together.

iii) The phonon band at 200 cm^{-1} (Figure 4C) is absent in Γ and arises from calculation of phonon dispersion. The mode is associated to the in-phase elongation of the Mg-Cl bonds in layer L_0 towards the inter-layer region, coupled with a single Mg-Cl elongation occurring in the adjacent layer L_{-1}.

iv) The band at 236 cm^{-1} (Figure 4D) is mainly due to the vibrational modes involving $MgCl_6$ moieties with a bulk hexa-coordinated Mg^{2+} cation (i.e. Mg_1). Starting from the frame where magnesium and four chlorine atoms lie in the same plane a pyramidalization at Mg_1 occurs with a consequent inversion of the $MgCl_4$ "umbrella" with Mg_1 atom passing again through the planar frame. Also atoms of adjacent layers are involved albeit at a less significant extent. It turns out that these vibrational modes involve the movement of atoms of the inner layers of the supercell model.

v) Finally, considering the axis formed by the axial chlorine ligands at hexacoordinated Mg atoms, the band at 251 cm^{-1} (Figure 4E) is mainly due to the rotation of that axis respect to the *ab* plane (i.e. the axis formed by Cl_4 Cl_5 bound to Mg_1 into L_0 layer). A coupling with rotations of opposite chlorine atoms in Mg-Cl-Mg-Cl cycles in upper and lower layers is observed (i.e. Cl_8Cl_9 axis in L_1 layer respect to the *ab* plane). The tilting four-membered Mg-Cl-Mg-Cl ring, which is almost a ubiquitous topological '*leit motiv*' of halides of alkaline earths, is present in the bulk (intralayer), but is also part of the penta-coordinated surfaces. Hence, at a qualitative level it is worth saying that this band might originate from the atomic vibrations of both inner and surface atoms (see following section). The displacements here described cause the movement of chlorine atoms along the *c* axis, i.e. parallel to the stacking direction.

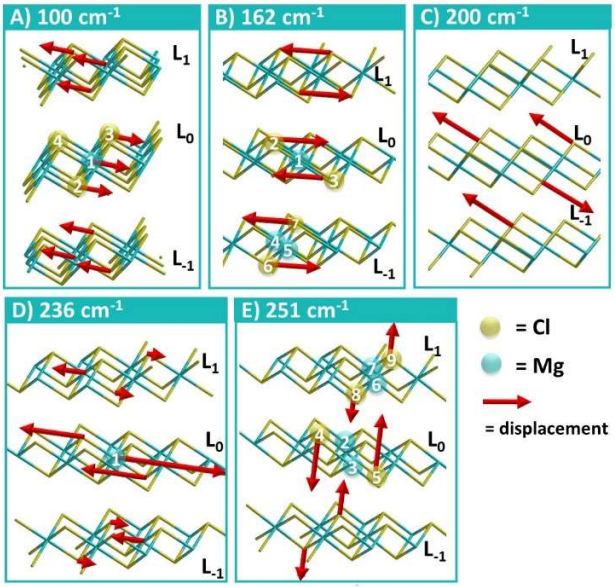

Figure 4. Graphical representation of normal modes associated to main phonon bands of ordered α-$MgCl_2$. Mg atoms are represented in green whereas chlorine atoms are in yellow; arrows showing direction of the atomic displacements (in red) have been added to help reader in visualize the vibrational modes. The labels are explained in the text.

Experiments reveal that the bands mostly affected by ball milling are those at 200 and 236 cm^{-1}, which decrease in intensity of about 25% from $MgCl_2$ A to $MgCl_2$ B and still a little bit more from $MgCl_2$ B to $MgCl_2$ C, and that at 251 cm^{-1}, which gradually reduces in intensity of about 10% at each step. The band at 162 cm^{-1}, instead, slightly downward shifts.

To elucidate the origin of these changes in the experimental INS spectra, the effect of disorder of bulk $MgCl_2$ was investigated. Figure 5 shows the neutron-weighted DOS simulated for the δ_{trans} (Figure 5A) and δ_{rot} (Figure 5B) models, compared to that of ordered α-$MgCl_2$. The experimental spectra are also reported as references (Figure 5C). The INS spectra of the disordered models are quite similar to that of the ordered one. To better appreciate the small changes, difference spectra δ_{trans}-α and δ_{rot}-α are reported in Figure 5A' and Figure 5B', respectively. At a first inspection, it can be observed that the introduction of a stacking fault or of a rotational fault causes a variation in either the position or the intensity (or both) of all the main bands. As far as the decrease in intensity is concerned, the ΔNWPDOS spectra are of the same order of magnitude of the experimental ΔS(Q, ω) spectrum (Figure 5C'), corresponding to a maximum of 10% with respect to the intensity of the spectrum of ordered $MgCl_2$. Actually, none of the ΔNWPDOS spectra are able to reproduce the experimental ΔS(Q, ω) spectrum. However, at a glance some bands look more sensitive to the translational disorder while some others are more affected by the rotational one. The two bands most influenced by translational disorder are those at 162 cm^{-1}, which upward shifts, and that at 236 cm^{-1}, which decreases in intensity. Both bands are associated with vibrational modes involving atoms displacements in the *ab* plane. Rotational disorder, instead, has a larger impact on the bands at 200 and 251 cm^{-1}, which decrease in intensity with respect to the spectrum of the bulk α phase. Both bands are ascribed to vibrational modes involving atoms displacements along the *c* axis.

By analogy, a description of the experimental ΔS(Q, ω) spectra in terms of combination of translational and rotational disorder can be attempted. On the one hand, the decrease in intensity of the two bands at 200 and 251 cm^{-1} that can be observed in both Figures 5C' and 5B' may indicate the occurrence of some rotational disorder. On the other hand, the decrease in intensity of the band at 236 cm^{-1} and the shift in position of the band at 162 cm^{-1} suggest that ball milling (see Figures 5A' and 5C') could also induce a certain degree of translational disorder. It is worth noticing that the direction of the shift for the band at 162 cm^{-1} predicted by our δ_{trans} model is the opposite of that observed experimentally. However, this might be due to the fact that δ_{trans} contains a single stacking fault, while in the real case the number of stacking faults can be higher and/or a stacking fault can be adjacent to a rotational fault. Indeed, the mode at 162 cm^{-1} is associated to the displacement of atoms in three adjacent layers. There are some major fluctuations in Figures 5A' and 5B' that cannot be seen in Figure 5C'. Those are likely due to some combination of defects of different types: rotational and translational ones but maybe also to some combination of disorder with surface effects (e.g. steps or edges). Figure 5C' reports the integral effect of both the rotational and translational disorder summed over many possible faults in stacking and combination of them while simulation refers to two possible models. Nevertheless, the global effect consists in a reduction/increase of intensity of some peaks but also the shift and broadening of bands i.e. the one close to 160 cm^{-1} is to some extent visible in both experimental and simulated difference spectra. The reproduction of the experimental ΔS(Q, ω) spectrum would require the simulation of a very large number of models with a different percentage of stacking and rotational faults, which is clearly not possible. Overall, the data displayed in Figure 5 indicate that INS is sensitive to the introduction of both translational and rotational disorder in $MgCl_2$ bulk.

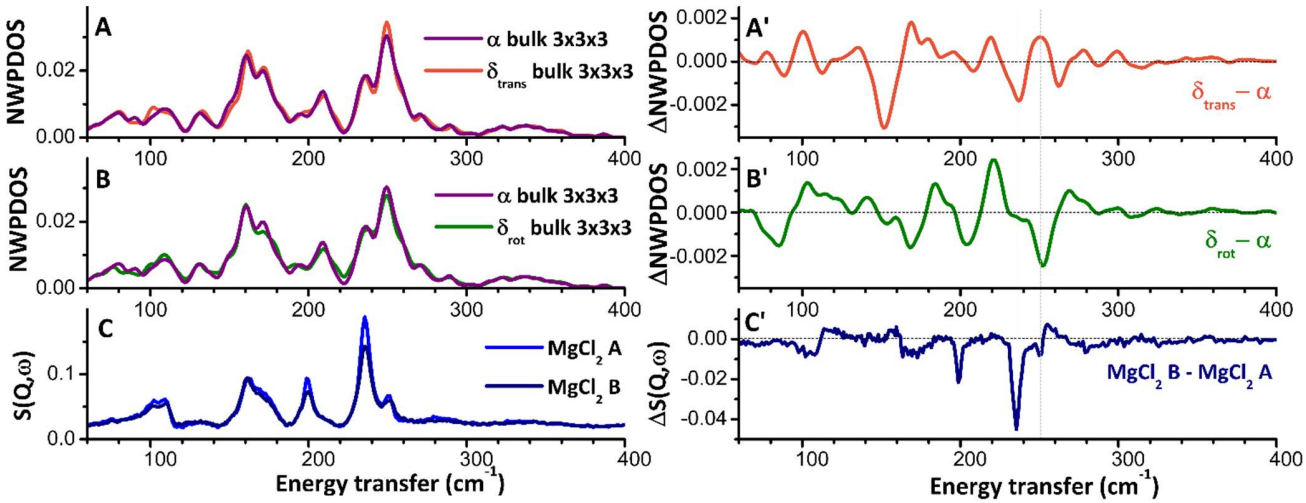

Figure 5. Neutron-weighted PDOS simulated for ordered bulk α-$MgCl_2$ and disordered δtrans (part A) and δrot (part B) forms by means of 3×3×3 supercells, compared to the experimental INS spectra of $MgCl_2$ A, $MgCl_2$ B and $MgCl_2$ C (part C). Difference simulated spectra Δ calculated by subtracting the spectrum of ordered bulk α-$MgCl_2$ to those of δ_{trans} (part A') and δrot (part B'), compared to the difference experimental spectrum calculated by subtracting that of $MgCl_2$ A from that of $MgCl_2$ B and the spectrum of $MgCl_2$ B from $MgCl_2$ C (part C').

4.4 Prediction of INS spectra for $MgCl_2$ surfaces

It is worthy to recall that for polar compounds and ionic crystals the long range character of Coulomb interaction causes the force constants to remain large, even when the atoms are far away. For this reason it is impossible to obtain a finer sampling of the reciprocal space just by means of Fourier interpolation and a computational cheap solution is the Wang correction cited above for three-dimensional systems.

Therefore, due to the ionic nature of $MgCl_2$ material, for lower dimensionality systems as 2-D and 1-D models (surface/rods), where long-range electrostatic contributions to the force constants are accounted through a direct approach, the slow decay of Coulomb interactions with atomic distances required the adoption of sufficiently large supercells to guarantee reliable (i.e. well-converged) scattering simulations. We checked convergence in results of scattering behaviour of bi-dimensional lattices as a function of super-cell size, ending in the identification of 4×4 supercells as provider of valuable prediction of the INS spectra. Accordingly, supercells of different size (i.e. 2×2, 4×4, 8×4, 8×8) have been adopted for phonon dispersion calculations. To provide a measure of the size of the supercells adopted as surface models, the (104) surfaces contain a number of atoms ranging from 192 [4×4] to 768 [8×8]. Further computational details are reported in Table S-2 in Supporting Information. It was found that 4×4 supercells provide reliable predictions of the INS spectra; more extended systems did not show any significant difference in simulated phonon density of states. It turns out that cell parameters corresponding to values close to the "critical dimension" of 12 Å are large enough to guarantee converged results i.e. to obtain a valuable sampling of the reciprocal space and long range effects.

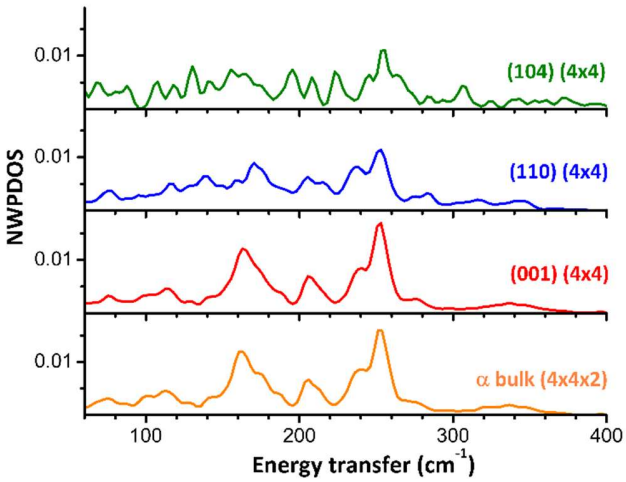

Figure 6. Neutron-weighted corrected DOS simulated for surfaces of α-$MgCl_2$ of interest in catalysis (i.e. (104) and (110)) and the basal one (i.e. (001)), compared to that simulated for ordered bulk α-$MgCl_2$.

For 2-D models having a 4×4 supercell the simulated INS spectra are reported in Figure 6, and compared to the spectrum simulated for the ordered bulk α-$MgCl_2$ (4×4×2 supercell). The INS spectrum of the basal (001) surface almost coincides with that of the bulk. The simulated INS spectra for the (104) and (110) surfaces, instead, are less intense than that of the basal plane and characterized by a series of additional vibrational modes below 200 cm^{-1}. In the 220 – 260 cm^{-1} region, the spectrum of the (104) surface displays a band at ~251 cm^{-1}, whereas there are no significant contributions to the peak at ~236 cm^{-1}. The spectrum of the (110) surface shows both bands at 251 and 236 cm^{-1}, but they show a different relative intensity with respect to those of the (001) basal one.

Overall, according to the data reported in Figure 6, the (104) and (110) surfaces do not contribute to the INS spectrum of $MgCl_2$ with specific features different from those of the (001) basal one, but eventually only with a poorly defined and weak band in the 100 – 200 cm^{-1} region. This means that, for $MgCl_2$ particles with lateral size of approximately 10-15 nm whose morphology is dominated by the basal plane (like those obtained by ball milling), INS is not expected to provide information on the morphology of the particles (i.e. on the exposed surfaces). The scenario might change for smaller $MgCl_2$ particles approaching the size of ca. 1 nm, where the relative contribution of surfaces different from the basal one can be higher, especially in the presence of capping agents (as it happens for chemically activated Ziegler-Natta pre-catalysts).

4.5 Prediction of INS spectra for 1-D periodic and 0-D $MgCl_2$ models

The presence of edges in nano-sized $MgCl_2$ has been simulated by the (110)/(104) rod (Figure 2C). The corresponding INS spectrum is shown in Figure 7. The intensity of the overall spectrum is even lower than for the (104) and (110) surfaces and it is hard to identify distinctive features. Only two bands at 247 and 260 cm^{-1} slightly emerge from the continuum, which are shifted towards higher frequencies with respect to the two bands at 236 and 251 cm^{-1} dominating the spectrum of bulk $MgCl_2$.

Finally, to investigate the effect of nano-sizing on the INS spectrum of $MgCl_2$, a nano-cluster containing 240 atoms and exposing surfaces according to the Wulff polyhedron predicted for $MgCl_2$ [3,26] has been cut out from the bulk. The simulated INS spectrum is also shown in Figure 7. Its overall intensity is comparable to that of the (104)/(110) rod and also in this case only two bands at 252 and 265 cm^{-1} clearly emerge from the continuum.

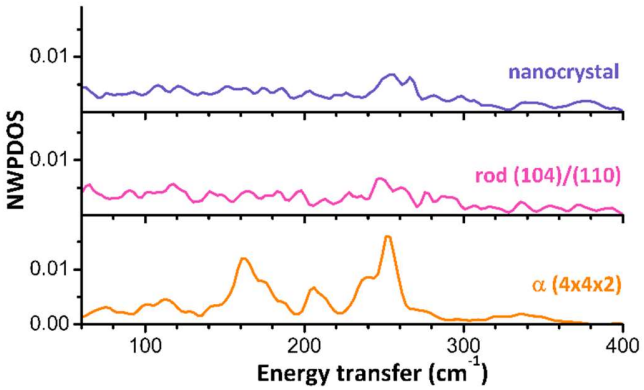

Figure 7. Neutron-weight corrected DOS simulated for α-MgCl2, a (110/104) rod, and a $MgCl_2$ nanocrystal.

Overall, the data shown in Figure 7 clearly demonstrate that nano-sizing of $MgCl_2$ (i.e. reduction of the particle size and increasing importance of edges) causes a drastic decrease in intensity of the overall INS spectrum, the disappearance of the features below 200 cm^{-1} characteristic for the bulk, and an upward shift of the features around 250 cm^{-1}. In other word, a key feature of nano-sizing is the loss of all the INS spectral features characteristic for $MgCl_2$ bulk and the rise of a couple of weak bands around 260 cm^{-1}, which have no direct relation with the surfaces terminating the crystal, but rather are connected with the vibrational properties of the edges.

5. Conclusions

The INS spectra of ball-milled $MgCl_2$ samples have been measured for the first time in order to investigate the disorder and nanosizing effects, which are relevant when $MgCl_2$ is used as support for Ziegler-Natta catalysts. Indeed, Cl shows a total scattering cross section that makes it a suitable target for the INS and allows better understanding of atomic motion with respect to typical IR and Raman vibrational spectroscopies.

In order to assign the bands observed in the experimental spectra and deepen the understanding of structural disorder and nano-sizing effects in these systems, the INS spectra have been simulated for 3-D models containing stacking or rotational disorder and for models of decreasing dimensionality (from 2-D to 0-D models).

The experimental results have shown that the bands mostly affected by ball milling are those at 200 cm^{-1}, 236 cm^{-1}, and 251 cm^{-1}, which gradually reduce in intensity upon ball milling. These changes can be rationalized in terms of an increase of the structural disorder. In particular, according to the computed results and simulated INS spectra, the decrease in intensity of the bands at 200 and 251 cm^{-1} (which are assigned to the vibrational modes involving atoms displacement along the *c* axis) indicates the occurrence of some rotational disorder, while the decrease in intensity of the band at 236 cm^{-1} (which is assigned to the vibrational modes involving atoms displacement in the *ab*

plane) suggests that ball milling induces also a certain degree of translational disorder. This is clear evidence that the INS measurements are sensitive to the introduction of disorder in bulk $MgCl_2$.

For 2D atomistic models well converged simulated phonon density of states are obtained for cell parameters corresponding to values close to 12÷15 Å. Notably, the INS spectrum of the basal (001) surface almost coincides with that of the bulk. Since $MgCl_2$ particles with lateral size of about 10-15 nm (like those obtained by ball milling) are dominated by the basal plane, INS is not expected to provide information on the morphology of the particles (i.e. on the exposed surfaces). This picture might change for $MgCl_2$ particles approaching the size of ca. 1 nm, where the relative contribution of surfaces different from the basal one can be higher, especially in the presence of adsorbates like in Ziegler-Natta pre-catalysts obtained with chemical activation methods. However, it is important to underline that our calculations performed on 1-D and 0-D models clearly indicate that a key feature of nano-sizing is the loss of the entire INS spectral features characteristic of $MgCl_2$ bulk.

In conclusion, our modelling provides a full rationale of the trends observed in the experimental INS spectra of samples of $MgCl_2$ with different degrees of ball-milling. The ball-milling process leads mostly to the formation of bulk-like $MgCl_2$ crystallites rather than nanoparticles. The weak bonding among $MgCl_2$ layers allows for an easier cleavage along the stacking direction with the emergence of both rotational and translational disorder, which explain the decrease in intensity of some bands in the INS spectrum, while nano-sizing effects are less evident.

We briefly underline some key-features of INS spectroscopy as applied to $MgCl_2$ materials, in comparison to other vibrational spectroscopies and structural methods. Far-IR spectra were found to be sensitive to the morphology of the $MgCl_2$ nanoparticles, revealing the type and the relative extension of exposed surfaces, but almost insensitive to $MgCl_2$ disorder. A previous Raman study[79] did not even assign some peaks (i.e. ~100 cm^{-1}). Beyond the field of spectroscopy, we proved in previous papers that the combination of PXRD, PDF, and relative simulation, have the potential to provide information on the dimension and disorder of δ-$MgCl_2$ in $MgCl_2$ supported Ziegler-Natta catalysts. The results discussed in the present work demonstrate that INS mimics the X-ray ability to reveal different types of disorder, as well as surfaces/borders effects for objects at the nanoscale.

In perspective, besides the interest in the field of Ziegler-Natta catalysis, the present work paves the route to the use of INS as a method for the characterization of materials with a certain degree of defectivity and shows the central role of quantum mechanical simulations for a correct interpretation and valorization of the experimental INS spectra.

ASSOCIATED CONTENT

Supporting Information. Details on the adopted models. Information on the adopted computational methodology and basis set effect. Influence of overtones and higher-order effects on simulated INS spectrum of $MgCl_2$. Neutron-weight corrected DOS simulated for both α and β polymorph of $MgCl_2$ at 0 K.

This material is available free of charge via the Internet at http://pubs.acs.org.

AUTHOR INFORMATION

Corresponding Author

* maddalena.damore@unito.it;

ORCID: orcid.org/0000-0002-4248-8767.

Department of Chemistry and NIS Centre, University of Turin, Via P. Giuria 7, 10125 Torino, Italy;

Contributions

The manuscript was written thanks to the contributions of all authors.

ACKNOWLEDGMENT

We kindly acknowledge PRACE initiative for computing resources (Grant: Project **2016163997**). ISIS Rutherford Appleton Laboratory UKRI, NScD Oak Ridge National Laboratory, European Spallation for experiments and SCARF Scientific Computing Department, STFC Rutherford Appleton Laboratory for computer facilities. The work of A.P. and E.G. forms part of the research program of DPI, project #802. Toru Wada, Gentoku Takasao, Ashutosh Thakur, Patchanee Chammingkwan, Minoru Terano, Toshiaki Taniike are kindly acknowledged for useful discussions on structural disorder effects of investigated systems. Dr. Jeff Armstrong ISIS Rutherford Appleton Laboratory is kindly acknowledged for careful reading of the manuscript.

REFERENCES

(1) Behrens, M.; Studt, F.; Kasatkin, I.; Kühl, S.; Hävecker, M.; Abild-Pedersen, F.; Zander, S.; Girgsdies, F.; Kurr, P.; Kniep, B. L.; Tovar, M.; Fischer, R. W.; Nørskov, J. K.; Schlögl, R. The Active Site of Methanol Synthesis over Cu/ZnO/Al2O 3 Industrial Catalysts. *Science* **2012**, 336 (6083), 893-897. https://doi.org/10.1126/science.1219831.

(2) Zecchina, A.; Groppo, E.; Bordiga, S. Selective Catalysis and Nanoscience: An Inseparable Pair. *Chem. - A Eur. J.* **2007**, *13* (9), 2440–2460. https://doi.org/10.1002/chem.200600678.

(3) D'Amore, M.; Causà, M. Extracting NanoRods and NanoCrystals from Bulk: http://tutorials.crystalsolutions.eu/tutorial.html?td=tuto_nano&tf=nano_md_g2.

(4) Evarestov, R. A. *Theoretical Modeling of Inorganic Nanostructures: Symmetry and Ab-Initio Calculations of Nanolayers, Nanotubes and Nanowires*; Springer-Verlag Berlin Heidelberg, 2015.

(5) *Catalysis and Electrocatalysis at Nanoparticle Surfaces*; Wieckowski, A., Savinova, E., Vayenas, C., Ed.; CRC Press, 2003. https://doi.org/10.1201/9780203912713.

(6) Pal, M.; Serrano, J. G.; Santiago, P.; Pal, U. Size-Controlled Synthesis of Spherical TiO_2 Nanoparticles: Morphology, Crystallization, and Phase Transition. *J. Phys. Chem. C* **2007**, *111* (1), 96–102. https://doi.org/10.1021/jp0618173.

(7) Kawasaki, H. Surfactant-Free Solution-Based Synthesis of Metallic Nanoparticles toward Efficient Use of the Nanoparticles' Surfaces and Their Application in Catalysis and Chemo-/Biosensing. *Nanotechnol. Rev.* **2013**, *2* (1), 5–25. https://doi.org/10.1515/ntrev-2012-0079.

(8) Wang, C.; Tian, W.; Ding, Y.; Ma, Y. Q.; Wang, Z. L.; Markovic, N. M.; Stamenkovic, V. R.; Daimon, H.; Sun, S. Rational Synthesis of Heterostructured Nanoparticles with Morphology Control. *J. Am. Chem. Soc.* **2010**, *132* (18), 6524–6529. https://doi.org/10.1021/ja101305x.

(9) Thushara, K. S.; D'Amore, M.; Piovano, A.; Bordiga, S.; Groppo, E. The Influence of Alcohols in Driving the Morphology of Magnesium Chloride Nanocrystals. *ChemCatChem* **2017**, *9* (10), 1782–1787. https://doi.org/10.1002/cctc.201700101.

(10) Bell, A. T. The Impact of Nanoscience on Heterogeneous Catalysis. *Science.* **2003**, *299* (5613), 1688–1691. https://doi.org/10.1126/science.1083671.

(11) Wulff, G. Zur Frage Der Geschwindigkeit Des Wachstums Undder Auflosung Der Krystallflachen. *Z. Kristallogr. Minerals* **1901**, *34*, 449.

(12) Herring, C. *The Physics of Powder Metallurgy*; Kingston, W. E., Ed.; McGraw-Hill, New York, 1951.

(13) Henry, C. R. Morphology of Supported Nanoparticles. *Prog. Surf. Sci.* **2005**, *80* (3–4), 92–116. https://doi.org/10.1016/j.progsurf.2005.09.004.

(14) Harris, P. J. F. Sulphur-Induced Faceting of Platinum Catalyst Particles. *Nature* **1986**, *323* (6091), 792–794. https://doi.org/10.1038/323792a0.

(15) Neumaier, M.; Weigend, F.; Hampe, O.; Kappes, M. M. Binding Energy and Preferred Adsorption Sites of CO on Gold and Silver-Gold Cluster Cations: Adsorption Kinetics and Quantum Chemical Calculations. *Faraday Discuss.* **2008**, *138*, 393–406. https://doi.org/10.1039/b705043g.

(16) Roldan Cuenya, B.; Behafarid, F. Nanocatalysis: Size- and Shape-Dependent Chemisorption and Catalytic Reactivity. *Surf. Sci. Rep.* **2015**, *70* (2), 135–187. https://doi.org/10.1016/j.surfrep.2015.01.001.

(17) Gao, F.; Zhang, Y.; Song, P.; Wang, J.; Yan, B.; Sun, Q.; Li, L.; Zhu, X.; Du, Y. Shape-Control of One-Dimensional PtNi Nanostructures as Efficient Electrocatalysts for Alcohol Electrooxidation. *Nanoscale* **2019**, *11* (11), 4831–4836. https://doi.org/10.1039/c8nr09892a.

(18) Combe, N.; Jensen, P.; Pimpinelli, A. Changing Shapes in the Nanoworld. *Phys. Rev. Lett.* **2000**, *85* (1), 110–113. https://doi.org/10.1103/PhysRevLett.85.110.

(19) Schapotschnikow, P.; Pool, R.; Vlugt, T. J. H. Molecular Simulations of Interacting Nanocrystals. *Nano Lett.* **2008**, *8* (9), 2930–2934. https://doi.org/10.1021/nl8017862.

(20) Henry, C. R. Surface Studies of Supported Model Catalysts. *Surf. Sci. Rep.* **1998**, *31* (7–8), 231–233. https://doi.org/10.1016/S0167-5729(98)00002-8.

(21) Yacamän, M. J.; OcañA Z., T. High-resolution Dark-field Electron Microscopy of Small Metal Particles. *Phys. Status Solidi* **1977**, *42* (2), 571–577. https://doi.org/10.1002/pssa.2210420220.

(22) Galli, P.; Barbè, P.; Guidetti, G.; Zannetti, R.; Martorana, A.; Marigo, A.; Bergozza, M.; Fichera, A. The Activation of MgCl2-Supported Ziegler-Natta Catalysts: A Structural Investigation. *Eur. Polym. J.* **1983**, *19* (1), 19–24. https://doi.org/10.1016/0014-3057(83)90096-4.

(23) Zannetti, R.; Marega, C.; Marigo, A.; Martorana, A. Layer-lattices in Ziegler–Natta Catalysts. *J. Polym. Sci. Part B Polym. Phys.* **1988**, *26* (12), 2399–2412. https://doi.org/10.1002/polb.1988.090261202.

(24) Martorana, A.; Zannetti, R.; Marigo, A.; Ajò, D.; Malta, V. PROVA, a Program for the Calculation of X-Ray Powder Spectra (Ordered and Disordered Structures). *Comput. Phys. Commun.* **1982**, *27* (1), 49–55. https://doi.org/10.1016/0010-4655(82)90006-6.

(25) Sementa, L.; D'Amore, M.; Barone, V.; Busico, V.; Causa', M. A Quantum Mechanical Study of $TiCl_3$ α, β and γ Crystal Phases: Geometry, Electronic Structure and Magnetism. *Phys. Chem. Chem. Phys.* **2009**, *11* (47), 11264–11275. https://doi.org/10.1039/b917013h.

(26) Wada, T.; Takasao, G.; Piovano, A.; D'Amore, M.; Thakur, A.; Chammingkwan, P.; Bruzzese, P. C.; Terano, M.; Civalleri, B.; Bordiga, S.; Groppo, E.; Taniike, T. Revisiting the Identity of δ-$MgCl_2$: Part I. Structural Disorder Studied by Synchrotron X-Ray Total Scattering. *J. Catal.* **2020**, *385*, 76–86. https://doi.org/10.1016/j.jcat.2020.03.002.

(27) Piovano, A.; D'Amore, M.; Wada, T.; Cleto Bruzzese, P.; Takasao, G.; Thakur, A.; Chammingkwan, P.; Terano, M.; Civalleri, B.; Bordiga, S.; Taniike, T.; Groppo, E. Revisiting the Identity of δ-$MgCl_2$: Part II. Morphology and Exposed Surfaces Studied by Vibrational Spectroscopies and DFT Calculation. *J. Catal.* **2020**, *387*, 1–11. https://doi.org/10.1016/j.jcat.2020.04.017.

(28) Bozyigit, D.; Yazdani, N.; Yarema, M.; Yarema, O.; Lin, W. M. M.; Volk, S.; Vuttivorakulchai, K.; Luisier, M.; Juranyi, F.; Wood, V. Soft Surfaces of Nanomaterials Enable Strong Phonon Interactions. *Nature* **2016**, *531* (7596), 618–622. https://doi.org/10.1038/nature16977.

(29) Mitchell, P. C. H.; Parker, S. F.; Ramirez-Cuesta, A.; Tomkinson, J. *Vibrational Spectroscopy with Neutrons, with Applications in Chemistry, Biology, Materials Science and Catalysis*; World Scientific Publishing Co. Pte. Ltd., 2005.

(30) Parker, S. F.; Collier, P. Applications of Neutron Scattering in Catalysis. *Johnson Matthey Technol. Rev.* **2016**, *60* (2), 132–144. https://doi.org/10.1595/205651316X691230.

(31) Pinna, R. S.; Rudić, S.; Parker, S. F.; Armstrong, J.; Zanetti, M.; Škoro, G.; Waller, S. P.; Zacek, D.; Smith, C. A.; Capstick, M. J.; McPhail, D. J.; Pooley, D. E.; Howells, G. D.; Gorini, G.; Fernandez-Alonso, F. The Neutron Guide Upgrade of the TOSCA Spectrometer. *Nucl. Instruments Methods Phys. Res. Sect. A Accel. Spectrometers, Detect. Assoc. Equip.* **2018**, *896*, 68–74. https://doi.org/10.1016/j.nima.2018.04.009.

(32) Arrigo, R.; Badmus, K.; Baletto, F.; Boeije, M.; Brinkert, K.; Bugaev, A.; Bukhtiyarov, V.; Carosso, M.; Catlow, R.; Chutia, A.; Davies, P.; De Leeuw, N.; Dononelli, W.; Freund, H. J.; Friend, C.; Gates, B.; Genest, A.; Hargreaves, J.; Hutchings, G.; Johnston, R.; Lamberti, C.; Marbaix, J.; Miranda, C. R.; Odarchenko, Y.; Richards, N.; Russell, A.; Selvam, P.; Sermon, P.; Shah, P.; Shevlin, S.; Shozi, M.; Skylaris, C. K.; Soulantica, K.; Torrente-Murciano, L.; Trunschke, A.; Van Santen, R.; Verga, L. G.; Whiston, K.; Willock, D. Theory as a Driving Force to Understand Reactions on Nanoparticles: General Discussion. *Faraday Discuss.* **2018**, *208*, 147–185. https://doi.org/10.1039/C8FD90013B.

(33) Bertini, F.; Glatz, M.; Stöger, B.; Peruzzini, M.; Veiros, L. F.; Kirchner, K.; Gonsalvi, L. Carbon Dioxide Reduction to Methanol Catalyzed by Mn(I) PNP Pincer Complexes under Mild Reaction Conditions. *ACS Catal.* **2019**, *9* (1), 632–639. https://doi.org/10.1021/acscatal.8b04106.

(34) Parker, S. F. Spectroscopy and Bonding in Ternary Metal Hydride Complexes-Potential Hydrogen Storage Media. *Coord. Chem. Rev.* **2010**, *254* (3–4), 215–234. https://doi.org/10.1016/j.ccr.2009.06.016.

(35) O'Malley, A. J.; Parker, S. F.; Catlow, C. R. A. Neutron Spectroscopy as a Tool in Catalytic Science. *Chem. Commun.* **2017**, *53* (90), 12164–12176. https://doi.org/10.1039/c7cc05982e.

(36) McGreevy, R. L.; Mitchell, E. W. J. Collective Modes in Molten Alkaline Earth Chlorides: Iii. Inelastic Neutron Scattering from Molten $MgCl_2$ and $CaCl_2$. *J. Phys. C Solid State Phys.* **1985**, *18*, 1163–1178. https://doi.org/10.1088/0022-3719/18/6/011.

(37) Dovesi, R.; Orlando, R.; Erba, A.; Zicovich-Wilson, C. M.; Civalleri, B.; Casassa, S.; Maschio, L.; Ferrabone, M.; De La Pierre, M.; D'Arco, P.; Noël, Y.; Causà, M.; Rérat, M.; Kirtman, B. CRYSTAL14 : A Program for the *Ab Initio* Investigation of Crystalline Solids. *Int. J. Quantum Chem.* **2014**, *114* (19), 1287–1317.

(38) Erba, A.; Baima, J.; Bush, I.; Orlando, R.; Dovesi, R. Large-Scale Condensed Matter DFT Simulations: Performance and Capabilities of the CRYSTAL Code. *J. Chem. Theory Comput.* **2017**, *13* (10), 5019–5027. https://doi.org/10.1021/acs.jctc.7b00687.

(39) Dovesi, R.; Erba, A.; Orlando, R.; Zicovich-Wilson, C. M.; Civalleri, B.; Maschio, L.; Rérat, M.; Casassa, S.; Baima, J.; Salustro, S.; Kirtman, B. Quantum-Mechanical Condensed Matter Simulations with CRYSTAL. *Wiley Interdiscip. Rev. Comput. Mol. Sci.* **2018**, *8* (4), e1360. https://doi.org/10.1002/wcms.1360.

(40) Orlando, R.; Delle Piane, M.; Bush, I. J.; Ugliengo, P.; Ferrabone, M.; Dovesi, R. A New Massively Parallel Version of CRYSTAL for Large Systems on High Performance Computing Architectures. *J. Comput. Chem.* **2012**, *33*, 2276–2284. https://doi.org/10.1002/jcc.23072.

(41) Becke, A. Density-functional Thermochemistry. III. The Role of Exact Exchange. *J. Chem. Phys.* **1993**, *98*, 5648–5652.

(42) Grimme, S. Semiempirical GGA-Type Density Functional Constructed with a Long-Range Dispersion Correction. *J. Comput. Chem.* **2006**, *27* (15), 1787–1799. https://doi.org/10.1002/jcc.20495.

(43) Grimme, S.; Antony, J.; Ehrlich, S.; Krieg, H. A Consistent and Accurate Ab Initio Parametrization of Density Functional Dispersion Correction (DFT-D) for the 94 Elements H-Pu. *J. Chem. Phys.* **2010**, *132* (15), 5648–5652. https://doi.org/10.1063/1.3382344.

(44) Grimme, S. Accurate Description of van Der Waals Complexes by Density Functional Theory Including Empirical Corrections. *J. Comput. Chem.* **2004**, *25* (12), 1463–1473. https://doi.org/10.1002/jcc.20078.

(45) Civalleri, B.; Zicovich-Wilson, C. M.; Valenzano, L.; Ugliengo, P. B3LYP Augmented with an Empirical Dispersion Term (B3LYP-D*) as Applied to Molecular Crystals. *CrystEngComm* **2008**, *10* (4), 405–410. https://doi.org/10.1039/B715018K.

(46) Valenzano, L.; Noël, Y.; Orlando, R.; Zicovich-Wilson, C. M.; Ferrero, M.; Dovesi, R. Ab Initio Vibrational Spectra and Dielectric Properties of Carbonates: Magnesite, Calcite and Dolomite. *Theor. Chem. Acc.* **2007**, *117*, 991–1000. https://doi.org/10.1007/s00214-006-0213-2.

(47) Apra, E.; Causa, M.; Prencipe, M.; Dovesi, R.; Saunders, V. R. On the Structural Properties of NaCl: An Ab Initio Study of the B1-B2 Phase Transition. *J. Phys. Condens. Matter* **1993**, *5* (18), 2969–2976. https://doi.org/10.1088/0953-8984/5/18/019.

(48) D'Amore, M.; Credendino, R.; Budzelaar, P. H. M.; Causá, M.; Busico, V. A Periodic Hybrid DFT Approach (Including Dispersion) to $MgCl_2$-Supported Ziegler-Natta Catalysts - 1: TiCl 4 Adsorption on MgCl 2 Crystal Surfaces. *J. Catal.* **2012**, *286*, 103–110. https://doi.org/10.1016/j.jcat.2011.10.018.

(49) Credendino, R.; Busico, V.; Causà, M.; Barone, V.; Budzelaar, P. H. M.; Zicovich-Wilson, C. Periodic DFT Modeling of Bulk and Surface Properties of MgCl2. *Phys. Chem. Chem. Phys.* **2009**, *11* (30), 6525–6532. https://doi.org/10.1039/b905676a.

(50) Erba, A.; Baima, J.; Bush, I.; Orlando, R.; Dovesi, R. Large-Scale Condensed Matter DFT Simulations: Performance and Capabilities of the CRYSTAL Code. *J. Chem. Theory Comput.* **2017**, *13* (10), 5019–5027. https://doi.org/10.1021/acs.jctc.7b00687.

(51) Monkhorst, H. J.; Pack, J. D. Special Points for Brillouin-Zone Integrations. *Phys. Rev. B* **1976**, *13* (12), 5188–5192. https://doi.org/10.1103/PhysRevB.13.5188.

(52) Zicovich-Wilson, C. M.; Pascale, F.; Roetti, C.; Saunders, V. R.; Orlando, R.; Dovesi, R. Calculation of the Vibration Frequencies of α-Quartz: The Effect of Hamiltonian and Basis Set. *J. Comput. Chem.* **2004**, *25* (15), 1873–1881. https://doi.org/10.1002/jcc.20120.

(53) Pascale, F.; Zicovich-Wilson, C. M.; López Gejo, F.; Civalleri, B.; Orlando, R.; Dovesi, R. The Calculation of the Vibrational Frequencies of Crystalline Compounds and Its Implementation in the CRYSTAL Code. *J. Comput. Chem.* **2004**, *25* (6), 888–897. https://doi.org/10.1002/jcc.20019.

(54) Parlinski, K.; Li, Z. Q.; Kawazoe, Y. First-Principles Determination of the Soft Mode in Cubic ZrO_2. *Phys. Rev. Lett.* **1997**, *78* (21), 4063–4066. https://doi.org/10.1103/PhysRevLett.78.4063.

(55) Togo, A.; Oba, F.; Tanaka, I. First-Principles Calculations of the Ferroelastic Transition between Rutile-Type and $CaCl_2$-Type SiO_2 at High Pressures. *Phys. Rev. B - Condens. Matter Mater. Phys.* **2008**, *78* (13), 134106(9). https://doi.org/10.1103/PhysRevB.78.134106.

(56) Alfè, D. PHON: A Program to Calculate Phonons Using the Small Displacement Method. *Comput. Phys. Commun.* **2009**, *180* (12), 2622–2633. https://doi.org/10.1016/j.cpc.2009.03.010.

(57) Erba, A.; Ferrabone, M.; Orlando, R.; Dovesi, R. Accurate Dynamical Structure Factors from Ab Initio Lattice Dynamics: The Case of Crystalline Silicon. *J. Comput. Chem.* **2013**, *34* (5), 346–354. https://doi.org/10.1002/jcc.23138.

(58) Wang, Y.; Wang, J. J.; Wang, W. Y.; Mei, Z. G.; Shang, S. L.; Chen, L. Q.; Liu, Z. K. A Mixed-Space Approach to First-Principles Calculations of Phonon Frequencies for Polar Materials. *J. Phys. Condens. Matter* **2010**, *22* (20), 202201. https://doi.org/10.1088/0953-8984/22/20/202201.

(59) Peintinger, M. F.; Oliveira, D. V.; Bredow, T. Consistent Gaussian Basis Sets of Triple-Zeta Valence with Polarization Quality for Solid-State Calculations. *J. Comput. Chem.* **2013**, *34* (6), 451–459. https://doi.org/10.1002/jcc.23153.

(60) Carpenter, J. M.; Price, D. L. Correlated Motions in Glasses Studied by Coherent Inelastic Neutron Scattering. *Phys. Rev.* Lett. 1985, 54 (5), 441–443. https://doi.org/10.1103/PhysRevLett.54.441.

(61) Piovano, A. Inelastic Neutron Scattering Applied to Materials for Energy. In *EPJ Web of Conferences*; 2015; Vol. 104, p 01006. https://doi.org/10.1051/epjconf/201510401006.

(62) Baima, J.; Ferrabone, M.; Orlando, R.; Erba, A.; Dovesi, R. Thermodynamics and Phonon Dispersion of Pyrope and Grossular Silicate Garnets from *Ab Initio* Simulations. *Phys. Chem. Miner.* **2016**, *43* (2), 137–149. https://doi.org/10.1007/s00269-015-0781-6.

(63) Lucas, M. S.; Kresch, M.; Stevens, R.; Fultz, B. Phonon Partial Densities of States and Entropies of Fe and Cr in Bcc Fe-Cr from

Inelastic Neutron Scattering. *Phys. Rev. B - Condens. Matter Mater. Phys.* **2008**, 77 (18), 184303. https://doi.org/10.1103/PhysRevB.77.184303.

(64) Osborn, R.; Goremychkin, E. A.; Kolesnikov, A. I.; Hinks, D. G. Phonon Density of States in MgB2. *Phys. Rev. Lett.* **2001,** 87 (1), 017005. https://doi.org/10.1103/PhysRevLett.87.017005.

(65) Arnold, O.; Bilheux, J. C.; Borreguero, J. M.; Buts, A.; Campbell, S. I.; Chapon, L.; Doucet, M.; Draper, N.; Ferraz Leal, R.; Gigg, M. A.; Lynch, V. E.; Markvardsen, A.; Mikkelson, D. J.; Mikkelson, R. L.; Miller, R.; Palmen, K.; Parker, P.; Passos, G.; Perring, T. G.; Peterson, P. F.; Ren, S.; Reuter, M. A.; Savici, A. T.; Taylor, J. W.; Taylor, R. J.; Tolchenov, R.; Zhou, W.; Zikovsky, J. Mantid - Data Analysis and Visualization Package for Neutron Scattering and μ SR Experiments. *Nucl. Instruments Methods Phys. Res. Sect. A Accel. Spectrometers, Detect. Assoc. Equip.* **2014**. https://doi.org/10.1016/j.nima.2014.07.029.

(66) Colognesi, D.; Celli, M.; Cilloco, F.; Newport, R. J.; Parker, S. F.; Rossi-Albertini, V.; Sacchetti, F.; Tomkinson, J.; Zoppi, M. TOSCA Neutron Spectrometer: The Final Configuration. *Appl. Phys. A Mater. Sci. Process.* **2002**, *74*, s64–s66. https://doi.org/10.1007/s003390101078.

(67) Parker, S. F.; Fernandez-Alonso, F.; Ramirez-Cuesta, A. J.; Tomkinson, J.; Rudic, S.; Pinna, R. S.; Gorini, G.; Fernández Castañon, J. Recent and Future Developments on TOSCA at ISIS. In *Journal of Physics: Conference Series*; 2014; Vol. 554, p 012003. https://doi.org/10.1088/1742-6596/554/1/012003.

(68) Giunchi, G.; Allegra, G. Structural Disorder In Microcrystalline $MgCl_2$. *J. Appl. Crystallogr.* **1983**, *17* (3), 172–178. https://doi.org/10.1107/S0021889884011250.

(69) D'Amore, M.; Thushara, K. S.; Piovano, A.; Causà, M.; Bordiga, S.; Groppo, E. Surface Investigation and Morphological Analysis of Structurally Disordered MgCl2 and MgCl2/TiCl4 Ziegler-Natta Catalysts. *ACS Catal.* **2016**, *6* (9), 5786–5796. https://doi.org/10.1021/acscatal.6b00871.

(70) Brambilla, L.; Zerbi, G.; Nascetti, S.; Piemontesi, F.; Morini, G. Experimental and Calculated Vibrational Spectra and Structure of Ziegler-Natta Catalyst Precursor: 50/1 Comilled MgCl2-TiCl 4. *Macromol. Symp.* **2004**, *213*, 287–302. https://doi.org/10.1002/masy.200450926.

SYNOPSIS TOC

For Table of Contents Only